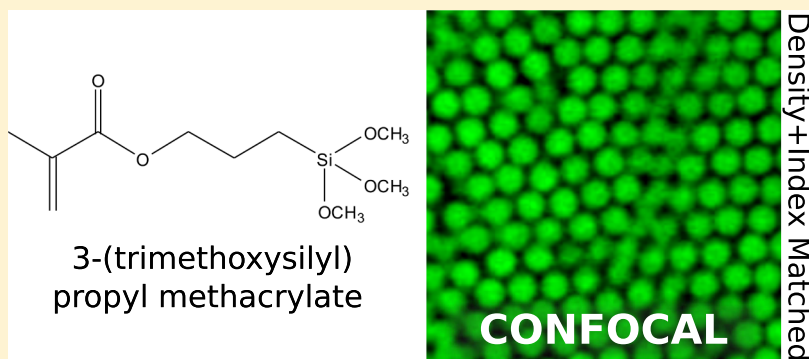


## Colloidal Organosilica Spheres for Three-Dimensional Confocal Microscopy

Yanyan Liu,<sup>†</sup> Taiki Yanagishima,<sup>†,§</sup> Arran Curran,<sup>†</sup> Kazem V. Edmond,<sup>†</sup> Stefano Sacanna,<sup>\*,‡</sup> and Roel P. A. Dullens<sup>\*,†</sup>

<sup>†</sup>Department of Chemistry, Physical and Theoretical Laboratory, University of Oxford, South Parks Rd., Oxford OX1 3QZ, U.K.

<sup>‡</sup>Molecular Design Institute, Department of Chemistry, New York University, New York 10003, United States



**ABSTRACT:** We describe the synthesis and application of 3-(trimethoxysilyl)propyl methacrylate (TPM) particles as a colloidal model system for three-dimensional (3D) confocal scanning laser microscopy. The effect of the initial TPM concentration on the growth and polydispersity of the particles and a recently developed solvent transfer method to disperse particles in a refractive index and density-matching solvent mixture are reviewed and discussed. To fully characterize the system as a colloidal model, we measure the pair potential between the TPM particles directly using optical tweezers. Finally, we use 3D confocal microscopy to image a sedimentation–diffusion equilibrium of TPM particles to characterize the phase behavior and particle dynamics through successful detection and tracking of all particles in the field of view.

### INTRODUCTION

Since Perrin's seminal experiment in the early 1900s,<sup>1</sup> colloidal particle suspensions have been widely used as physical models to study complex phase behavior. Given their easily accessible length and time scale, they have provided fundamental insight into the phase behavior of a wide range of condensed-matter phenomena.<sup>2,3</sup> With the development of three-dimensional (3D) imaging techniques such as confocal microscopy,<sup>4–6</sup> we have unprecedented access to the local processes involved in condensed matter phenomena such as crystallization,<sup>3,7</sup> glass formation,<sup>8–12</sup> gels,<sup>13–16</sup> interfacial phenomena,<sup>17,18</sup> and liquid-crystalline behavior.<sup>19–21</sup> By matching the colloidal particle's refractive index and density using solvent mixtures, real-space and time-resolved studies of the complex structural and dynamic properties of a colloidal model material can be performed with single-particle resolution.<sup>4,5,22</sup>

Currently, some of the most widely used colloidal model spheres include silica spheres,<sup>4</sup> polymethyl-methacrylate (PMMA) spheres,<sup>7,8,23</sup> and poly(*N*-isopropyl acrylamide) (PNIPAM) spheres.<sup>24</sup> PNIPAM allows in situ modification of volume fraction, thanks to its expansion/contraction under different temperatures and pH, but it exhibits significant particle softness in refractive index-matching solvents when swollen.<sup>25</sup> Fluorescent PMMA particles<sup>6,26,27</sup> are widely used,

but can be difficult to synthesize, largely because of the involved procedure for producing the poly(12-hydroxystearic acid) stabilizer required<sup>26,28,29</sup> and the swelling of the particles in the presence of haloalkanes. Silica particles<sup>4,30,31</sup> feature excellent chemical resistance, but density-matched suspensions are difficult to realize because of their high mass density. As such, studies in negligible gravity are limited to particles which are 10s or 100s of nanometers in size. This has led to a number of efforts over the years<sup>32–34</sup> to create different colloidal materials where monodisperse micron-sized particles may be synthesized and imaged in index-matching solvents.

Recently, microparticles made from 3-(trimethoxysilyl)-propyl methacrylate (TPM) have been introduced<sup>35–37</sup> which have a similar mid-range refractive index and density to that of PMMA. Structurally, TPM consists of an inorganic alkoxysilyl head group and a long organic methacrylate tail (Figure 1). This allows it to bond covalently to both inorganic and organic materials, making it an effective “bridging” material, and is therefore widely used as a coating reagent in polymer and surface chemistry.<sup>38,39</sup> As a fully cross-linked

**Received:** April 1, 2019

**Revised:** May 15, 2019

**Published:** May 16, 2019

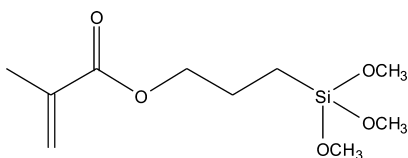


**Figure 1.** 3-(Trimethoxysilyl)propyl methacrylate.

colloidal particle, TPM is structurally stable in both polar and nonpolar solvents because of its combined silicon and carbon chemistry. Given the ease of its one-pot synthesis,<sup>37</sup> TPM provides a facile means to create a refractive index and density-matched colloidal system that can be used for 3D confocal microscopy.

Here, we describe a synthesis and characterization of spherical TPM particles aimed at optimizing the system presented in previous work<sup>37,40</sup> for quantitative confocal microscopy studies in three dimensions. First, we revisit the synthesis to ensure we reach the particle dimensions required for single-particle tracking, and that they are stably dispersed in index and density-matching solvents. Observation and sizing is carried out using confocal microscopy, static light scattering (SLS), and scanning electron microscopy (SEM). We then characterize the interparticle interaction, applying optical tweezing to directly measure the pair potential between spherical TPM particles in the solvent mixture; because the index was matched, we used a recently developed polystyrene (PS)–TPM core–shell particle<sup>41</sup> as an extremely close analogue to our TPM particles in terms of particle–particle interaction. Finally, we demonstrate its usage with quantitative 3D confocal scanning laser microscopy by observing the 3D sedimentation–diffusion profile of TPM particles in a refractive index-matching medium using confocal microscopy, studying the structure and dynamics at different depths.

## EXPERIMENTAL METHODS

**Materials.** TPM (Polysciences Inc.), ammonium hydroxide solution (28% vol  $\text{NH}_3$  in  $\text{H}_2\text{O}$ , Sigma-Aldrich,  $\geq 99.99\%$ ), and  $\alpha$ -azo-iso-butyronitrile (AIBN, BDH, UK) were used as supplied. The fluorescent monomer rhodamine B isothiocyanate aminopropyl trimethoxysilane (RITC-APS) was synthesized according to the procedure described by Ivell et al.<sup>42</sup> in dimethyl sulfoxide (DMSO, Sigma-Aldrich,  $\geq 99.5\%$ ), using rhodamine B isothiocyanate (Aldrich) and 3-aminopropyl trimethoxysilane (Aldrich, 97%). PEG–PPG–PEG Pluronic F108 (Aldrich) was used to make a 5% w/w aqueous mixture before being used in the experiments. The following solvents were supplied by Sigma-Aldrich and filtered using hydrophobic poly(tetrafluoroethylene) syringe filters (Millipore) with 0.45  $\mu\text{m}$  pore size before usage: ethanol ( $\geq 99.8\%$ ), 1,2,3,4-tetrahydronaphthalene or tetralin (99%) and trichloroethylene (TCE,  $\geq 99.5\%$ ). OLOA-1200 (Chevron Chemical Co.) was kindly supplied to us by Eric Dufresne; OLOA-11000 (Azelis) was kindly donated to us directly by the manufacturer (OLOA is a registered trademark of Chevron Oronite Company LLC, United States). Ultrapure water (type I) was used in the syntheses, and was obtained directly from a Direct-Q 3 UV purification system (Millipore).

**TPM Particle Synthesis.** Typically, a batch of monodisperse TPM particles is prepared in a 150 mL round-bottom flask. First, deionized water is mixed thoroughly with 0.1% v/v  $\text{NH}_4\text{OH}$  (aq) using a magnetic stirrer to obtain a homogeneous solution of  $\sim\text{pH}$  10. Care is taken to ensure that the flow profile inside the flask is steady and bubble-free, especially noting that the vortex in the middle is not in contact with the stirrer bar. Next, TPM oil is injected rapidly just below the solution surface and allowed to react for 45 min, continuing to stir at 500 rpm. Nucleation of the droplets can be seen around 5 min after the start of the reaction, as the mixture becomes increasingly

turbid. The course of the reaction is followed by taking 20  $\mu\text{L}$  samples from the reaction mixture and checked using bright field microscopy.

To prevent droplet coalescence in the subsequent fluorescence labeling step, Pluronic F108 surfactant can be added to stabilize the droplet surface. F108 solution (25  $\mu\text{L}$ ) (5% w/w) is introduced per 1 mL of the reaction mixture, equivalent to 0.125% w/w F108 overall. The TPM droplets are subsequently labeled with RITC-APS fluorescent monomers dissolved in DMSO. The dye is introduced in 100  $\mu\text{L}$  increments at 5 min intervals until the color of the mixture is fully saturated; typically, this takes 2 or 3 additions. Note that excess addition of the DMSO solution may lead to droplet coalescence. Finally, the droplets are polymerized into fully cross-linked particles by free-radical polymerization using AIBN. This is added in excess ( $\geq 3$  mM) and is stirred for 10 min before the reaction mixture is heated to 80  $^\circ\text{C}$  for 5 h in the oven.

The particles are cleaned in ultrapure water by repeated centrifugation, decanting, and redispersion with gentle sonication and stirring. Any residue or secondary TPM nuclei are removed by decanting the supernatant at least three times. The size and polydispersity of the particles are determined using a combination of light scattering techniques (ALV/CGS-3 compact goniometer) and SEM (JEOL LV6400).

**Solvent Transfer.** In order to apply confocal microscopy deep inside the bulk of a concentrated suspension, it is necessary to transfer the particles to a refractive index-matching solution, often composed of a mixture of organic solvents. This is presented in refs;<sup>21,41</sup> we describe the procedure in more detail in this paper. In the case of TPM, it was found that a mixture of tetralin and TCE may achieve index matching. However, simply centrifuging the particles and replacing the supernatant water causes irreversible aggregation because of the sudden change of polarity and demixing of the solvents. Thus, it was necessary to use an intermediate solvent, ethanol, which was miscible with both water and the organic solvent mixture. First, the particles were centrifuged to produce a stable pellet. Half of the supernatant was removed without disturbing the pellet, and the particles dispersed thoroughly using short bursts of vortex mixing and sonication. Next, ethanol was dripped in slowly (approx. 1 drip per second) while gently agitating the vial. This was achieved either manually, or by mounting the vial on a vortex at a low speed setting. After further vortexing and sonication, the mixture was recentrifuged to produce a stable pellet again. Now, all of the supernatant was removed and replaced with ethanol. Care was taken to thoroughly vortex and sonicate the particles to ensure they were properly redispersed in the new solvent. This process of redispersion, centrifugation, and supernatant removal was repeated at least five times to ensure thorough removal of any water. After five washing steps, it was found that leaving the TPM particles in ethanol in a sealed vial at slightly elevated temperatures (50–60  $^\circ\text{C}$ ) overnight helped to disperse the final traces of water into the ethanol medium. After one final washing step afterward, the particles were considered to have been fully transferred to ethanol. The sample was checked using bright field microscopy to ensure that no clustering could be seen.

Now, the same procedure as before was repeated with ethanol and a 1 wt % solution of OLOA in tetralin. OLOA is a stabilizer composed primarily of polyisobutene succinimide, and is known to be an effective charge control agent for colloidal particles in apolar solvents.<sup>43,44</sup> Both OLOA 1200 and OLOA 11000 were effective in stabilizing TPM in tetralin; all of the work presented below uses OLOA 1200. The sample was centrifuged, half of the supernatant removed, the particles redispersed, and the removed volume replaced dropwise with tetralin solution. This was followed by at least five cycles of washing with the tetralin solution interspersed with vortex mixing and sonication. The end result is a suspension of TPM particles in tetralin. In order to finally reach a mixture of tetralin and TCE, the particles may be centrifuged and the supernatant replaced with the desired composition, either directly or in steps.

**Confocal Microscopy.** The confocal microscopy experiments were carried out using a Thorlabs confocal 8 kHz resonant point scanner mounted on an Olympus IX73 microscope. The microscope

was equipped with an Olympus Plan Apochromat oil immersion objective with 60 times magnification and a numerical aperture of 1.42. For sedimentation experiments, a 45:55 mixture of tetralin to TCE (with 1 wt % OLOA 1200) was used, closely matching the refractive index while leaving a small enough density difference between the particles and the solvent to observe an extended sedimentation–diffusion profile. Typically,  $\sim 100\ \mu\text{L}$  of a 3% volume fraction suspension is injected into a glass sample chamber, consisting of a narrow channel and a resealable inlet, and is left to sediment for 2–3 days. To observe the sedimentation profile, confocal  $z$ -stacks of  $32 \times 28 \times 100\ \mu\text{m}^3$  are taken at 200 nm intervals in  $z$  using bidirectional scanning. When investigating particle dynamics, 3D time-series of  $32 \times 28 \times 20\ \mu\text{m}^3$  volumes were scanned for 400 frames over approximately 27 min. The  $z$ -spacing was increased to 250 nm to reduce the time taken to image each  $z$ -stack in the time series; this resulted in a scan time of 4 s per volume. Lastly, the 3D particle trajectories are extracted from the 3D confocal data using a standard particle-tracking algorithm.<sup>45</sup>

**Optical Trapping and Pair-Potential Measurement.** We use a recently developed PS–TPM core–shell system<sup>41</sup> to measure the interparticle interaction potential between TPM particles; while the outer shell layer is composed of the same TPM that makes up our particles, there is a high refractive index PS core, which allows for optical manipulation. Using 3D holographic optical tweezing on a recently developed apparatus with confocal imaging capability,<sup>46</sup> a pair of core–shell particles are moved to a position roughly  $30\ \mu\text{m}$  above the bottom cover glass to prevent wall effects. The laser intensity is adjusted, so that the particles are weakly trapped, and thermal fluctuations are visible. Subsequently, the distance between the optical traps is systematically varied by moving their position using a spatial light modulator.

The force acting on the particles may be determined through knowledge of the potential energy profile created by a trap. For small displacements from the trap center, single spherical particles are known to be confined via an approximately harmonic potential with a force constant  $\kappa$ . This parameter is measured by observing the thermal fluctuations of a single-trapped core–shell particle relative to the center of the trap over 10 min. The probability distribution for particle positions  $P(x)$  is related to the potential via the expression  $P(x) \approx \exp[-U_{\text{trap}}(x)/k_{\text{B}}T]$ . The recovered potential energy of a single particle in a single trap is given as an inset in Figure 3A. Fitting a quadratic  $U_{\text{trap}} = \frac{1}{2}\kappa x^2$ , we extract a trapping stiffness  $\kappa$ .

This parameter allows us to directly convert displacements of the particle from the trap center to a force, and thus a potential. The specific way in which this calculation was implemented is given in the Results and Discussion section. In the experiment, the separation between the two optical traps was set at regular intervals between 3.2 and  $4.4\ \mu\text{m}$ , and the trapping stiffness was kept at  $\kappa = (7.4 \pm 0.2) \times 10^{-7}\ \text{N m}^{-1}$ . Note that different pairs of particles would require recalibration of the trapping stiffness because of the polydispersity in the particle diameter. Confocal 2D cross sections through the centers of the core–shell particles are recorded at a frame rate of  $\sim 120$  frames per second using bidirectional resonant scanning over the course of 10 min for each trap separation. We emphasize that we use PS–TPM particles,<sup>41</sup> not pure TPM, enabling a unique measurement in which we measure the interaction between particles that do not have an index gradient with the solvent at their surfaces. However, it is reasonable to assume that the interaction between PS–TPM particles with a thick TPM shell is identical to that between pure TPM particles because of identical surface properties.

## RESULTS AND DISCUSSION

**TPM Particle Synthesis.** TPM particles of different sizes are synthesized by adjusting the initial TPM reagent concentration as described here<sup>37</sup> and shown in Figure 2A–C. Initial TPM concentrations of 93.5, 23.4 and 11.7 mM are investigated. The particle sizes and polydispersities are characterized using SLS and fitting with Mie-theory form

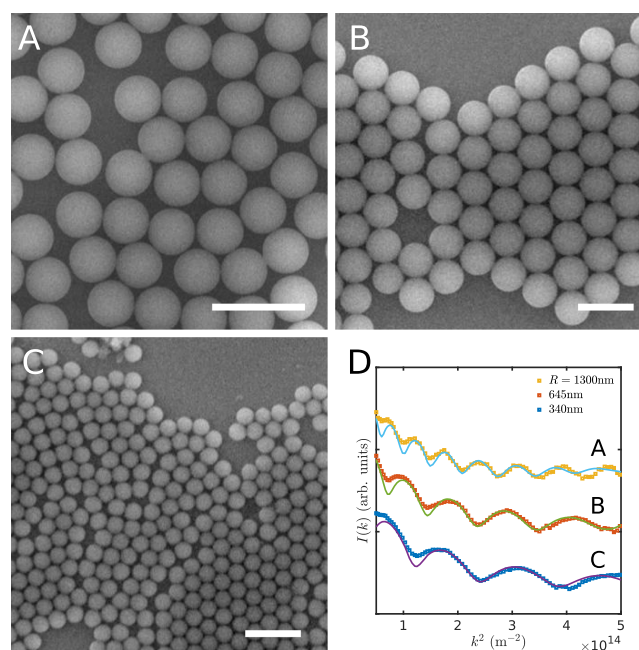


**Figure 2.** SEM images of cross-linked TPM particles with different starting TPM concentrations: (A)  $R = 1300\ \text{nm}$  (2.5% polydispersity), (B)  $R = 645\ \text{nm}$  (4%), (C)  $R = 340\ \text{nm}$  (8%). Scale bar is  $5\ \mu\text{m}$  for (A),  $2\ \mu\text{m}$  for (B,C). The radii  $R$  and polydispersities were determined using SLS, as shown in (D). Labels (A–C) on the data (points) and fits (lines) correspond to figures (A–C).

factors (Figure 2D). We observe that batches resulting in smaller particles had higher polydispersities at a given pH; this is consistent with findings in literature.<sup>37</sup> Importantly, it is clear that we are able to synthesize particles with a diameter of greater than  $1.5\text{--}2.0\ \mu\text{m}$ , allowing particle detection in dense suspensions from three-dimensional confocal image stacks.<sup>22,45</sup>

**Optical Trapping and Pair-Potential Measurement.** To be an effective colloidal model system, it is vital that the particles have a well-characterized interparticle pair potential. One might consider using an optical trapping setup to directly measure pairwise interactions,<sup>47,48</sup> but the system is refractive index-matched, leaving no index gradient to allow particle manipulation. Thus, we measured the particle–particle pair potential of PS–TPM particles in the same refractive index-matching solvent. As stated previously, while the PS core provides sufficient index contrast for optical trapping, the shell is identical in composition to pure TPM particles and thus, the nature of the interaction is expected to be extremely similar. The core–shell particles we used contained a  $1.8\ \mu\text{m}$  diameter PS core and had a total diameter of  $3.1\ \mu\text{m}$  with a polydispersity of 8%, measured using SLS in water. The volume fraction of particles in the sample is kept low, below 0.1%, to ensure facile isolation of a single pair of particles with no other particles near the field of view. The solvent was the same 45:55 mixture of tetralin to TCE (with 1 wt % OLOA 1200) used for the sedimentation–diffusion experiments (see below).

Pairs of PS–TPM core–shell particles were brought to different interparticle distances using optical trapping in the absence of other traps. The trapping potential is characterized as described above. In the absence of an interaction, the particles are expected to lie at the center of the traps, albeit subject to thermal fluctuations. We use this to account for any systematic error, which may shift the actual trap to trap



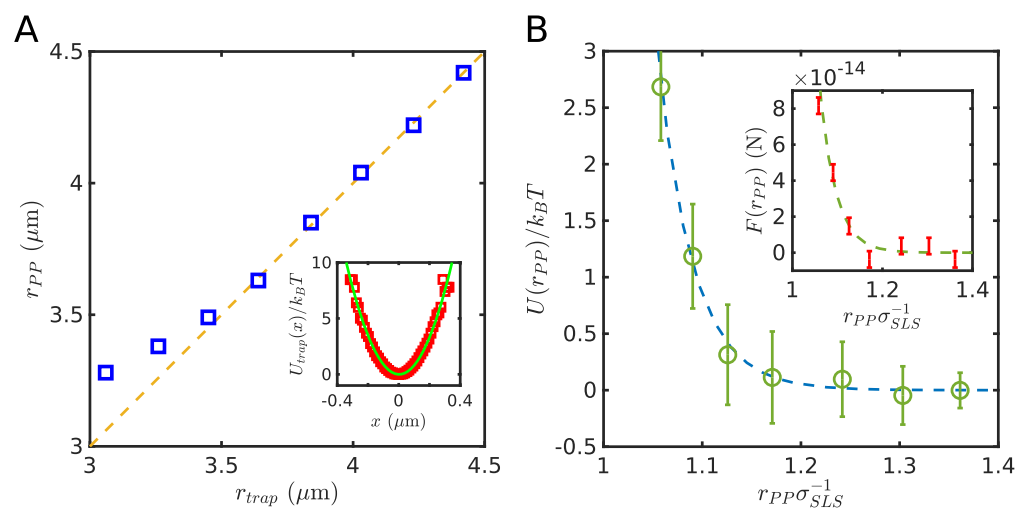


**Figure 3.** (A) Detected center-to-center separation between two core-shell particles  $r_{pp}$  as a function of the distance between the traps  $r_{trap}$ . A line  $r_{pp} = r_{trap}$  is included to highlight the deviation at small interparticle separations. Error bars are less than half the size of the markers. (Inset) Optical trapping potential for a single PS-TPM core-shell particle in a TPM refractive index-matching solvent, fitted with a parabola. Data is taken from the pair potential measurement experiment for  $r_{trap} = 4.4 \mu\text{m}$ . (B) Interaction potential of the core-shell particles, fitted with the hard-sphere Yukawa function (eq 1). Inset: The corresponding force curve as a function of  $r_{pp}$ . The particle diameter from SLS is  $\sigma_{SLS} = 3.1 \mu\text{m}$  for both (A,B). Errors are propagated from (A).

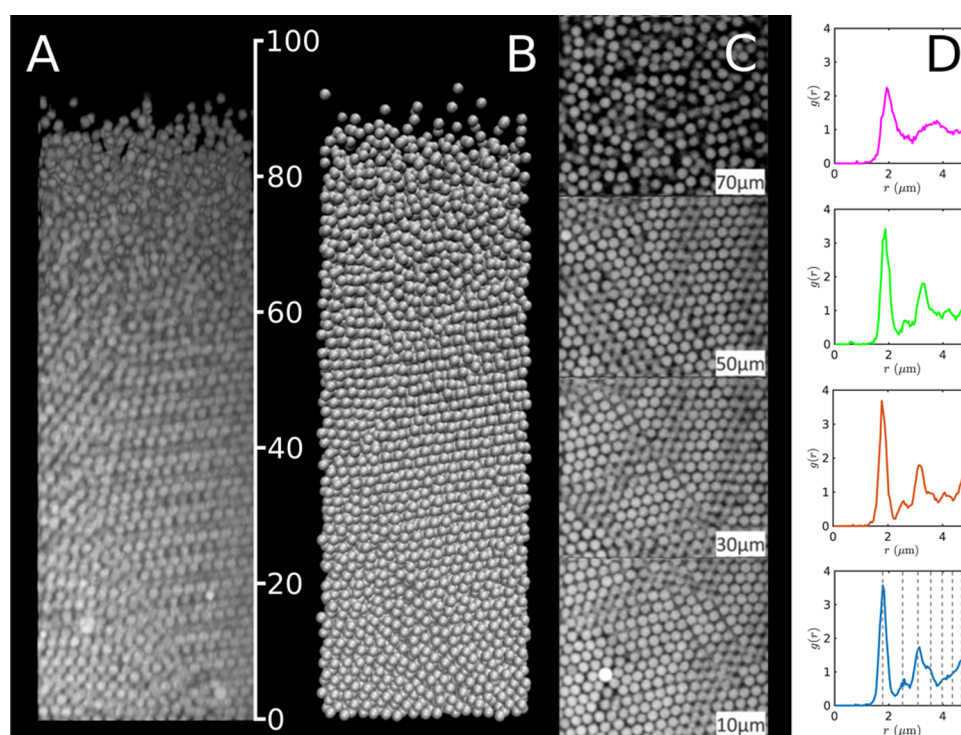


**Figure 4.** (A)  $x$ - $z$  plane of a 3D confocal image reconstruction of a TPM  $z$ -stack. (B) Rendering of particles at coordinates detected using a widely used 3D particle-tracking algorithm over the whole  $z$ -stack. Scale bar tick marks are given at  $20 \mu\text{m}$  intervals. (C) Single  $x$ - $y$  confocal slice images at different heights in  $z$  for the same data set as in (A). (D) Radial distribution functions  $g(r)$  for particles located in different  $z$  ranges; from the top to the bottom,  $60 < z < 80 \mu\text{m}$ ,  $40 < z < 60 \mu\text{m}$ ,  $20 < z < 40 \mu\text{m}$ , and  $0 < z < 20 \mu\text{m}$ . Known peak positions relative to the first peak for face-centered cubic structures are given in the lowest stack.

distance, and use this to derive an  $r_{trap}$ . Note that fluctuations in the apparent positions from this line can be used to estimate errors on the points; because of extensive averaging, this is approximately  $10 \text{ nm}$ , smaller than the size of the markers in the plot.

As the particles get closer, Figure 3A shows that  $r_{pp}$  and  $r_{trap}$  begin to deviate. This deviation can be used to derive the pair potential between the two particles; considering two identical

harmonic potentials with constant  $\kappa$ , a simple geometric argument shows that this deviation is related to the force  $F_{pp}(r)$  acting between the particles by  $F_{pp}(r) = \frac{1}{2}\kappa(r_{pp} - r_{trap})$ . The force is given as an inset in Figure 3B. Finally, the interaction potential may be obtained by integrating  $F_{pp}(r)$  using the expression  $U_{pp} = \int_{r_{\infty}}^r F_{pp}(r) dr$ . Errors are found by propagating the errors identified in Figure 3A.

The result is a smoothly varying repulsive interaction with a finite range, as expected from weakly charged particles suspended in a low dielectric constant solvent. TPM particles are known to exhibit a negative charge,<sup>37</sup> so it is plausible to expect that they exhibit a softness in their repulsion. To characterize the interparticle potential of a pair of charged particles, we fitted the plot with a Yukawa potential with a hard-sphere term.

$$\frac{U(r)}{k_B T} = \begin{cases} \frac{\epsilon \exp(-\kappa \sigma (r/\sigma - 1))}{r/\sigma} & \text{for } r > \sigma \\ \infty & \text{for } r \leq \sigma \end{cases} \quad (1)$$

The size parameter  $\sigma$  was set to the SLS particle size  $\sigma_{\text{SLS}} = 3.1 \mu\text{m}$ . The functional form of the fit shows agreement with the measured potential. Extrapolating to contact, where  $r\sigma^{-1} = 1$ , we obtain a contact value of  $\epsilon = 13.0$ , as well as a value for the Debye length in the refractive index-matching solvent of  $\kappa^{-1} = 118 \text{ nm}$ . Applying  $\kappa$  and  $\epsilon$  to the simulated phase diagrams of hard-sphere Yukawa systems as reported by Hynninen and Dijkstra,<sup>49</sup> the freezing transition for TPM particles in this refractive index-matching solvent is expected to occur in the range  $\phi \approx 0.37\text{--}0.41$ . We note that this range is taken from simulations at slightly higher and lower contact energies,<sup>49</sup> respectively.

Thus, we have demonstrated that TPM particles in an index-matching solvent mixture exhibit a well-characterized repulsive interaction with a Debye length consistent with previous studies of colloidal crystallization using charged PMMA particles.<sup>5,50</sup>

**Confocal Microscopy Study of Sedimentation–Diffusion Equilibrium.** As a result of the close refractive index-matching of the solvent medium with the TPM particles, we are able to image deep inside a colloidal suspension. We apply this capability to the observation of a sedimentation–diffusion equilibrium where the gravitational length of the particles is on the order of a particle diameter. In particular, we take 3D confocal microscopy stacks to track particles over a wide range of depths. An example is shown in Figure 4. A 3% volume fraction suspension of  $1.68 \mu\text{m}$  particles was sealed in a microscopy chamber and allowed to sediment overnight. Figure 4A displays a  $x$ – $z$  side-on view of the  $z$ -stack, showing the state of the system over  $100 \mu\text{m}$  in the  $z$ -direction. Particle coordinates extracted from Figure 4A can also be used to create a 3D digital rendering of the system, as shown in Figure 4B. Good correspondence can be seen between the raw image and the reconstruction over the entire  $z$  range.

To examine the phase behavior of the system as a function of height, we have also shown confocal snapshots of the  $x$ – $y$  plane at four different heights in this  $z$ -stack (see Figure 4C). It is clear from the confocal slices that the sample between  $0 < z < 60 \mu\text{m}$  is closely packed and crystalline. This is further demonstrated by computing the radial distribution function using particles located in  $20 \mu\text{m}$  thick subsection; from the top to the bottom, these ranges are  $60 < z < 80 \mu\text{m}$ ,  $40 < z < 60 \mu\text{m}$ ,  $20 < z < 40 \mu\text{m}$ , and  $0 < z < 20 \mu\text{m}$ . These are given to the right of the corresponding images. The crystalline layers show sharp second and third peaks in the  $g(r)$ , indicating a high degree of order in higher coordination shells. The position of the peaks shows good agreement with a face-centred cubic (FCC) structure; expected relative peak positions to the first peak for FCC are given as dotted lines in the bottom stack.

However, for  $z > 60 \mu\text{m}$ , there is a clear decrease in the ordering and the form of the  $g(r)$  is more fluid-like.

A plot of local volume fraction  $\phi(z)$  as a function of  $z$  is given in Figure 5. For  $z < 10 \mu\text{m}$ , oscillations are seen in  $\phi(z)$

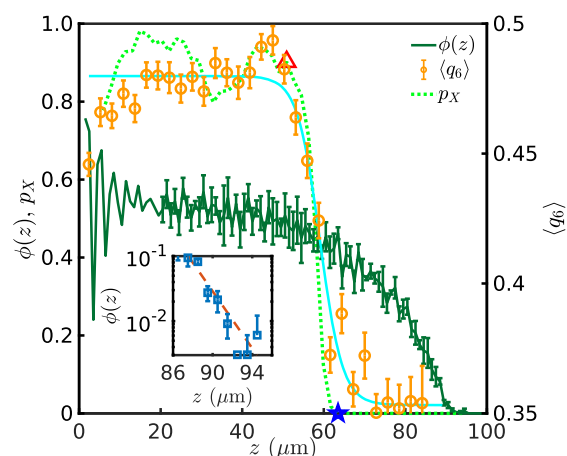


**Figure 5.** Volume fraction  $\phi$  and bond-orientational order parameter  $q_6$  as a function of  $z$  for the stack shown in Figure 4. The decay of  $q_6$  has been fitted with a hyperbolic tangent function. The thick dotted line shows the proportion of crystalline particles  $p_X$ ; markers have been placed for the freezing (blue star) and melting (red triangle) points. Error bars have been omitted from the layered region at low  $z$  for clarity. (Inset) Enlarged  $\phi(z)$  profile in the dilute limit, with a linear fit to the log–lin plot, used to extract the gravitational length.

because of the layering of the particles parallel to the bottom of the sample chamber, as seen previously.<sup>18</sup> Between  $10 < z < 50 \mu\text{m}$ , the volume fraction slowly decreases, corresponding to the crystalline phase observed in Figure 4. Between approximately  $50 < z < 85 \mu\text{m}$ , there is a slow decay in  $\phi(z)$  as we enter the dense fluid region of the stack. Above  $z = 85 \mu\text{m}$ , we see a sharp decay before the volume fraction falls to zero. Errors were estimated by splitting the imaged volume into four quadrants in  $xy$  and comparing profiles; note that error bars were omitted in the layered region for clarity.

Next, we quantify the degree of crystallinity of the system at different heights for a comparison with the phase behavior reported for hard-sphere Yukawa systems.<sup>49</sup> Given the availability of particle coordinates, the transition from the crystal phase to the fluid phase can be identified by calculating the local bond (Steinhardt) order parameter,  $q_6$ , as a function of  $z$ .<sup>51</sup> For a single-particle  $i$ , the local bond order parameter is defined as

$$q_6(i) = \sqrt{\frac{4\pi}{13} \sum_{m=-6}^6 |q_{6m}(i)|^2} \quad (2)$$

where

$$q_{6m}(i) = \frac{1}{N_b(i)} \sum_{j=1}^{N_b(i)} Y_{6m}(\mathbf{r}_{ij}) \quad (3)$$

Here,  $N_b(i)$  is the number of nearest neighbors for particle  $i$ , and  $\mathbf{r}_{ij}$  is the vector between particles  $i$  and  $j$ . Nearest neighbors are identified with a distance threshold corresponding to the first minimum of the local  $g(r)$ .  $Y_{6m}(\mathbf{r}_{ij})$  are spherical harmonics with integer values  $-6 \leq m \leq 6$ . Average values of  $q_6$  are taken over particles in different bins in  $z$  to obtain a profile of  $\langle q_6 \rangle$  as

a function of height. Errors are found from standard errors on the mean for each bin. Note that only one in three bins have been plotted in the figure, for extra clarity. This is superimposed on a profile of the local volume fraction  $\phi(z)$  in Figure 5 and fitted with a hyperbolic tangent function. Note that when  $\phi(z) \lesssim 0.10$ , it is difficult to unambiguously identify the nearest neighbors required to find  $q_6$ ; thus,  $q_6$  values when  $\phi(z) \lesssim 0.10$  are omitted from the plot and hyperbolic tangent fit. The choice of function is empirical. The crystal phase, coexistence phase, and fluid phase are very clear in Figure 5. Between  $0 < z < 50 \mu\text{m}$ , the  $\langle q_6 \rangle(z)$  profile appears mostly flat and takes a high value, indicating a high degree of crystalline order. Between  $50 < z < 70 \mu\text{m}$ , there is a large drop in  $\langle q_6 \rangle(z)$ , indicating decreasing crystallinity, and the incidence of the coexistence region. For  $z < 70 \mu\text{m}$ , there is a short persistence of  $\langle q_6 \rangle(z)$  around 0.35, before the incidence of a dilute gaseous phase around  $z = 80 \mu\text{m}$ . For comparison, we associate the midpoint of the drop in  $\langle q_6 \rangle_z$  with the mid-point between freezing and melting points; this occurs at  $59 \mu\text{m}$ , which corresponds to a local  $\phi \approx 0.42$ . This is inconsistent with the  $\phi_{\text{mid}} \approx 0.52$  of a hard-sphere system, once again indicating a soft, charged interparticle interaction in our system. This freezing point is in fact approximately consistent with what is expected from our pair-potential measurements; particles with the Debye length and interaction strength we measured are expected to have a freezing point in the range  $\phi = 0.37\text{--}0.41$  and a melting point in the range  $\phi = 0.40\text{--}0.45$ .<sup>49</sup>

We may also attempt a more rigorously defined identification of crystalline particles by using the metric described in ref 52, where particles are only considered crystalline if they have more than a threshold number of nearest neighbors with the same phase in the complex value of  $q_6$ . This value is often termed bond coherence, defined as  $d_{6ij} = \sum_{m=6}^{m=6} q_{6m}(i) q_{6m}^*(j) / |q_{6m}(i)| |q_{6m}(j)|$  for neighboring particles  $i$  and  $j$ . If  $d_{6ij}$  is greater than 0.7, the pair of particles are both considered “solid” neighbors to each other. Particles with 7 or more “solid” neighbors are finally considered crystalline. The proportion of crystalline particles  $p_x$  at different heights has been superimposed on Figure 5, showing a sharp transition from liquid to solid phases at the freezing point (marked with a blue star). Considering a smoothed density profile  $\phi(z)$  near the interface, we find that the freezing point is located at  $\phi_f \approx 0.41$ , marked with a blue star. This is consistent with the range found in simulations.<sup>49</sup> We may also attempt to approximate the plateau value for  $p_x$  at high volume fraction and locate a melting point  $\phi_m$ , marked with a red triangle; it is worth noting that this is much less accurate than finding the freezing point because the grain structure and layering both lead to a fluctuating plateau. We find  $\phi_m = 0.48$ , which agrees roughly with simulations,<sup>49</sup> where the melting point is in the range  $0.40\text{--}0.45$ .

At the other end of the profile, where the particle concentration is low ( $\phi \rightarrow 0$ ), it is known that the particle distribution can be described using the Boltzmann distribution as a function of height

$$\phi(z) = \phi_0 \exp\left(-\frac{z}{z_0}\right) \quad (4)$$

Here,  $\phi_0$  is the packing fraction at  $z = 0$ , and  $z_0$  is the gravitational length. This tail in the density profile is shown as an inset in Figure 5 for clarity; we may apply eq 4 as demonstrated in ref 53 and perform a linear fit to the log-lin

plot to extract the gravitational length  $z_0$  (also shown in the inset), expressed as

$$z_0 = \frac{k_B T}{(\Delta\rho) \left(\frac{4}{3}\pi R^3\right) g} \quad (5)$$

where  $\Delta\rho$  is the mass density difference between the particle and the medium,  $R$  is the particle radius, and  $g$  is the acceleration due to gravity. Once  $z_0$  is known, the mass density of the TPM particles can be calculated. We obtain a value of  $z_0 = 1.98 \mu\text{m}$  for the TPM sample. From these, we estimate the mass density of the TPM particles to be  $1.29 \text{ g cm}^{-3}$ . This is consistent with measurements for the TPM particles synthesized by van der Wel et al.<sup>37</sup>

**Particle Dynamics at Different Heights.** Finally, we demonstrate a study of the single-particle dynamics of TPM particles observed with 3D confocal microscopy. Changes in the volume fraction of the TPM particles as a function of height can also greatly influence the diffusive dynamics of the particles,<sup>8,54,55</sup> as we indeed see by examining the mean squared displacement (MSD) of particles at different heights in the sample. We use the same particle data shown in Figure 4A in four different height ranges:  $10 < z < 30 \mu\text{m}$ ,  $30 < z < 50 \mu\text{m}$ ,  $50 < z < 70 \mu\text{m}$ , and  $70 < z < 90 \mu\text{m}$ . Note that different ranges from those in the previous figure have been chosen to avoid the effect of the wall. These span all the phases in the system, allowing for clear comparison between dynamics and the structure. The MSDs were calculated directly from the particle trajectories using

$$\langle r^2(t) \rangle = \frac{1}{N} \sum_{i=1}^N \langle |\mathbf{r}_i(t) - \mathbf{r}_i(0)|^2 \rangle \quad (6)$$

where  $N$  is the number of particles, and  $\mathbf{r}_i$  is the position of particle  $i$ . These are shown in Figure 6; the average packing fractions  $\phi$  for each of the curves are given in the plot legend.

Because of limited imaging speed, we were unable to probe the MSD for  $t < 3 \text{ s}$ . Errors were found by taking the  $y$  intercept of a linear fit to the MSD<sup>56</sup> when  $\phi = 0.27$ , taking the

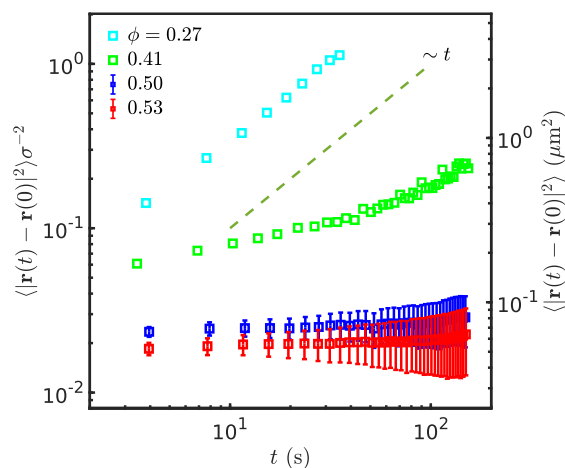


**Figure 6.** MSD of particles at different volume fractions, corresponding to four different positions in the sedimentation–diffusion equilibrium profile shown in Figure 4. The average packing fractions  $\phi$  for each of the substacks are given in the plot legend. From the top plot to the bottom,  $z$  ranges are  $10 < z < 30 \mu\text{m}$ ,  $30 < z < 50 \mu\text{m}$ ,  $50 < z < 70 \mu\text{m}$ , and  $70 < z < 90 \mu\text{m}$ .



number of independent intervals sampled for each lag time into consideration. Note that these were smaller than the plot markers for the two lowest volume fractions. From Figure 6, we see that particles become increasingly diffusive for lower volume fraction. On the other hand, for  $10 < z < 30 \mu\text{m}$  ( $\phi = 0.53$ ), and  $30 < z < 50 \mu\text{m}$  ( $\phi = 0.50$ ), the MSD profiles are flat. From Figure 4C,D and the  $\langle q_6 \rangle$  analysis, the sample is crystalline between  $10 < z < 50 \mu\text{m}$ . This is consistent with the plateau in the MSD, as particles are strongly confined by their neighbours. However, for  $50 < z < 70 \mu\text{m}$  ( $\phi = 0.41$ ), where the packing fraction is near the freezing transition, the MSD is now subdiffusive. This indicates that more particles can escape the cage formed by their neighbors, but the confinement effect still exists, albeit transiently, analogous to what one might see in a supercooled liquid.<sup>57</sup> There is also a slight upward trend near the end of the MSD, suggesting a recovery of diffusivity at larger time scales. For particles in the more dilute fluid region between  $70 < z < 90 \mu\text{m}$  ( $\phi = 0.27$ ), the MSD is fully diffusive, as expected. Importantly, we confirm that our TPM particles may be imaged over time using 3D confocal scanning microscopy to achieve single-particle tracking in the liquid phase.

## CONCLUSIONS

In summary, we have developed and characterized a refractive-index and density-matched colloidal model system that is suitable for 3D confocal laser scanning microscopy studies with single-particle resolution. The TPM colloidal particles have been characterized using bright-field microscopy, SLS and SEM. We directly determined the pair-potential between TPM particles in the same index-matching solvent, which is well described by a Yukawa interaction. We have also examined the sedimentation–diffusion equilibrium of the TPM model system and successfully imaged both the structure and dynamics of the colloids over a wide range of local packing fractions, reconciling characteristics of the interparticle potential and the phase behavior.

## AUTHOR INFORMATION

### Corresponding Authors

\*E-mail: [s.sacanna@nyu.edu](mailto:s.sacanna@nyu.edu) (S.S.).

\*E-mail: [roel.dullens@chem.ox.ac.uk](mailto:roel.dullens@chem.ox.ac.uk) (R.P.A.D.).

### ORCID

Taiki Yanagishima: 0000-0002-7511-1958

Stefano Sacanna: 0000-0002-8399-3524

### Notes

The authors declare no competing financial interest.

§Previous Address: Institute of Industrial Science, The University of Tokyo, Japan.

## ACKNOWLEDGMENTS

We acknowledge the European Research Council (ERC) for financial support (Starting Grant 279541-IMCOLMAT and Consolidator Grant 724834-OMCIDC). Y.L. and R.P.A.D. acknowledge SCG Chemicals Co. Ltd. for financial support. T.Y. acknowledges the support of the Japan Society for the Promotion of Science through the Grant-in-Aid for JSPS Research Fellows (16J06649). S.S. acknowledges support from NSF-CAREER award DMR-1653465. We thank Dirk Aarts for fruitful discussions. We acknowledge Eric Dufresne and Azelis for their provision of the OLOA stabiliser.

## REFERENCES

- (1) Perrin, J.; Hammick, D. L. *Atoms*; Ox Bow Press, 1923.
- (2) Lu, P. J.; Weitz, D. A. Colloidal Particles: Crystals, Glasses, and Gels. *Annu. Rev. Condens. Matter Phys.* **2013**, *4*, 217–233.
- (3) Palberg, T. Crystallization kinetics of colloidal model suspensions: recent achievements and new perspectives. *J. Phys.: Condens. Matter* **2014**, *26*, 333101.
- (4) van Blaaderen, A.; Wiltzius, P. Real-Space Structure of Colloidal Hard-Sphere Glasses. *Science* **1995**, *270*, 1177–1179.
- (5) Gasser, U.; Weeks, E. R.; Schofield, A.; Pusey, P. N.; Weitz, D. A. Real-Space Imaging of Nucleation and Growth in Colloidal Crystallization. *Science* **2001**, *292*, 258–262.
- (6) Prasad, V.; Semwogerere, D.; Weeks, E. R. Confocal microscopy of colloids. *J. Phys.: Condens. Matter* **2007**, *19*, 113102.
- (7) Pusey, P. N.; van Megen, W. Phase behaviour of concentrated suspensions of nearly hard colloidal spheres. *Nature* **1986**, *320*, 340–342.
- (8) Kegel, W. K.; van Blaaderen, A. Direct Observation of Dynamical Heterogeneities in Colloidal Hard-Sphere Suspensions. *Science* **2000**, *287*, 290–293.
- (9) Weeks, E. R.; Crocker, J. C.; Levitt, A. C.; Schofield, A.; Weitz, D. A. Three-dimensional direct imaging of structural relaxation near the colloidal glass transition. *Science* **2000**, *287*, 627–631.
- (10) Simeonova, N. B.; Dullens, R. P. A.; Aarts, D. G. A. L.; de Villeneuve, V.; Lekkerkerker, H.; Kegel, W. K. Devitrification of colloidal glasses in real space. *Phys. Rev. E: Stat., Nonlinear, Soft Matter Phys.* **2006**, *73*, 041401.
- (11) Jensen, K. E.; Weitz, D. A.; Spaepen, F. Local shear transformations in deformed and quiescent hard-sphere colloidal glasses. *Phys. Rev. E: Stat., Nonlinear, Soft Matter Phys.* **2014**, *90*, 042305.
- (12) Weeks, E. R. Introduction to the colloidal glass transition. *ACS Macro Lett.* **2017**, *6*, 27–34.
- (13) Lu, P. J.; Zaccarelli, E.; Ciulla, F.; Schofield, A. B.; Sciortino, F.; Weitz, D. A. Gelation of particles with short-range attraction. *Nature* **2008**, *453*, 499–503.
- (14) Van Schooneveld, M. M.; De Villeneuve, V. W. A.; Dullens, R. P. A.; Aarts, D. G. A. L.; Leunissen, M. E.; Kegel, W. K. Structure, stability, and formation pathways of colloidal gels in systems with short-range attraction and long-range repulsion. *J. Phys. Chem. B* **2009**, *113*, 4560–4564.
- (15) Zupkauskas, M.; Lan, Y.; Joshi, D.; Ruff, Z.; Eiser, E. Optically transparent dense colloidal gels. *Chem. Sci.* **2017**, *8*, 5559–5566.
- (16) Tsurusawa, H.; Russo, J.; Leocmach, M.; Tanaka, H. Formation of porous crystals via viscoelastic phase separation. *Nat. Mater.* **2017**, *16*, 1022–1028.
- (17) Aarts, D. G. A. L.; Schmidt, M.; Lekkerkerker, H. N. W. Direct visual observation of thermal capillary waves. *Science* **2004**, *304*, 847–850.
- (18) Dullens, R. P. A.; Aarts, D. G. A. L.; Kegel, W. K. Dynamic broadening of the crystal-fluid interface of colloidal hard spheres. *Phys. Rev. Lett.* **2006**, *97*, 228301.
- (19) Mukhija, D.; Solomon, M. J. Nematic order in suspensions of colloidal rods by application of a centrifugal field. *Soft Matter* **2011**, *7*, 540.
- (20) Kuijk, A.; Imhof, A.; Verkuijlen, M. H. W.; Besseling, T. H.; Van Eck, E. R. H.; Van Blaaderen, A. Colloidal silica rods: Material properties and fluorescent labeling. *Part. Part. Syst. Char.* **2014**, *31*, 706–713.
- (21) Fernández-Rico, C.; Yanagishima, T.; Curran, A.; Aarts, D. G. A. L.; Dullens, R. P. A. Synthesis of Colloidal SU-8 Polymer Rods Using Sonication. *Adv. Mater.* **2019**, *31*, 1807514.
- (22) Leocmach, M.; Tanaka, H. A novel particle tracking method with individual particle size measurement and its application to ordering in glassy hard sphere colloids. *Soft Matter* **2013**, *9*, 1447–1457.
- (23) Kodger, T. E.; Lu, P. J.; Wiseman, G. R.; Weitz, D. A. Stable, Fluorescent Polymethylmethacrylate Particles for the Long-Term

Observation of Slow Colloidal Dynamics. *Langmuir* **2017**, *33*, 6382–6389.

(24) Peng, Y.; Wang, F.; Wang, Z.; Alsayed, A. M.; Zhang, Z.; Yodh, A. G.; Han, Y. Two-step nucleation mechanism in solid-solid phase transitions. *Nat. Mater.* **2015**, *14*, 101–108.

(25) Senff, H.; Richtering, W. Temperature sensitive microgel suspensions: Colloidal phase behavior and rheology of soft spheres. *J. Chem. Phys.* **1999**, *111*, 1705–1711.

(26) Bosma, G.; Pathmamanoharan, C.; de Hoog, E. H. A.; Kegel, W. K.; van Blaaderen, A.; Lekkerkerker, H. N. W. Preparation of Monodisperse, Fluorescent PMMA-Latex Colloids by Dispersion Polymerization. *J. Colloid Interface Sci.* **2002**, *245*, 292–300.

(27) Dullens, R. P. A.; Claesson, M.; Derks, D.; Van Blaaderen, A.; Kegel, W. K. Monodisperse Core–Shell Poly(methyl methacrylate) Latex Colloids. *Langmuir* **2003**, *19*, 5963–5966.

(28) Elsesser, M. T.; Hollingsworth, A. D. Revisiting the synthesis of a well-known comb-graft copolymer stabilizer and its application to the dispersion polymerization of poly(methyl methacrylate) in organic media. *Langmuir* **2010**, *26*, 17989–17996.

(29) Royall, C. P.; Poon, W. C. K.; Weeks, E. R. In search of colloidal hard spheres. *Soft Matter* **2013**, *9*, 17–27.

(30) van Blaaderen, A.; Vrij, A. Synthesis and Characterization of Colloidal Dispersions of Fluorescent, Monodisperse Silica Spheres. *Langmuir* **1992**, *8*, 2921–2931.

(31) Verhaegh, N. A. M.; Blaaderen, A. v. Dispersions of Rhodamine-Labeled Silica Spheres: Synthesis, Characterization, and Fluorescence Confocal Scanning Laser Microscopy. *Langmuir* **1994**, *10*, 1427–1438.

(32) Koenderink, G. H.; Sacanna, S.; Pathmamanoharan, C.; Raşa, M.; Philipse, A. P. Preparation and properties of optically transparent aqueous dispersions of monodisperse fluorinated colloids. *Langmuir* **2001**, *17*, 6086–6093.

(33) Klein, S. M.; Manoharan, V. N.; Pine, D. J.; Lange, F. F. Preparation of monodisperse PMMA microspheres in nonpolar solvents by dispersion polymerization with a macromonomeric stabilizer. *Colloid Polym. Sci.* **2003**, *282*, 7–13.

(34) Kodger, T. E.; Guerra, R. E.; Sprakel, J. Precise colloids with tunable interactions for confocal microscopy. *Sci. Rep.* **2015**, *5*, 14635.

(35) Sacanna, S.; Irvine, W. T. M.; Chaikin, P. M.; Pine, D. J. Lock and key colloids. *Nature* **2010**, *464*, 575–578.

(36) Sacanna, S.; Irvine, W. T. M.; Rossi, L.; Pine, D. J. Lock and key colloids through polymerization-induced buckling of monodisperse silicon oil droplets. *Soft Matter* **2011**, *7*, 1631–1634.

(37) van der Wel, C.; Bhan, R. K.; Verweij, R. W.; Frijters, H. C.; Gong, Z.; Hollingsworth, A. D.; Sacanna, S.; Kraft, D. J. Preparation of Colloidal Organosilica Spheres through Spontaneous Emulsification. *Langmuir* **2017**, *33*, 8174–8180.

(38) Novak, B. M. Hybrid Nanocomposite Materials?between inorganic glasses and organic polymers. *Adv. Mater.* **1993**, *5*, 422–433.

(39) Zhang, K.; Chen, H.; Chen, X.; Chen, Z.; Cui, Z.; Yang, B. Monodisperse Silica-Polymer Core-Shell Microspheres via Surface Grafting and Emulsion Polymerization. *Macromol. Mater. Eng.* **2003**, *288*, 380–385.

(40) Middleton, C.; Hannel, M. D.; Hollingsworth, A. D.; Pine, D. J.; Grier, D. G. Optimizing the Synthesis of Monodisperse Colloidal Spheres Using Holographic Particle Characterization. *Langmuir* **2019**, *35* (20), 6602–6609.

(41) Liu, Y.; Edmond, K. V.; Curran, A.; Bryant, C.; Peng, B.; Aarts, D. G. A. L.; Sacanna, S.; Dullens, R. P. A. Core-Shell Particles for Simultaneous 3D Imaging and Optical Tweezing in Dense Colloidal Materials. *Adv. Mater.* **2016**, *28*, 8001–8006.

(42) Ivell, S. J.; Dullens, R. P. A.; Sacanna, S.; Aarts, D. G. A. L. Emerging structural disorder in a suspension of uniformly dimpled colloidal particles. *Soft Matter* **2013**, *9*, 9361–9365.

(43) Pugh, R. J.; Matsunaga, T.; Fowkes, F. M. The dispersibility and stability of carbon black in media of low dielectric constant. 1. Electrostatic and steric contributions to colloidal stability. *Colloids Surf.* **1983**, *7*, 183–207.

(44) Sainis, S. K.; Germain, V.; Mejean, C. O.; Dufresne, E. R. Electrostatic Interactions of Colloidal Particles in Nonpolar Solvents: Role of Surface Chemistry and Charge Control Agents†. *Langmuir* **2008**, *24*, 1160–1164.

(45) Crocker, J. C.; Grier, D. G. Methods of Digital Video Microscopy for Colloidal Studies. *J. Colloid Interface Sci.* **1996**, *179*, 298–310.

(46) Curran, A.; Tuohy, S.; Aarts, D. G. A. L.; Booth, M. J.; Wilson, T.; Dullens, R. P. A. Decoupled and simultaneous three-dimensional imaging and optical manipulation through a single objective. *Optica* **2014**, *1*, 223–226.

(47) Crocker, J. C.; Grier, D. G. Microscopic measurement of the pair interaction potential of charge-stabilized colloid. *Phys. Rev. Lett.* **1994**, *73*, 352–355.

(48) Polin, M.; Roichman, Y.; Grier, D. G. Autocalibrated colloidal interaction measurements with extended optical traps. *Phys. Rev. E: Stat., Nonlinear, Soft Matter Phys.* **2008**, *77*, 051401.

(49) Hynninen, A.-P.; Dijkstra, M. Phase diagrams of hard-core repulsive Yukawa particles. *Phys. Rev. E: Stat., Nonlinear, Soft Matter Phys.* **2003**, *68*, 021407.

(50) Arai, S.; Tanaka, H. Surface-assisted single-crystal formation of charged colloids. *Nat. Phys.* **2017**, *13*, 503–509.

(51) Lechner, W.; Dellago, C. Accurate determination of crystal structures based on averaged local bond order parameters. *J. Chem. Phys.* **2008**, *129*, 114707.

(52) Russo, J.; Tanaka, H. The microscopic pathway to crystallization in supercooled liquids. *Sci. Rep.* **2012**, *2*, 505.

(53) Royall, C. P.; Roij, R. v.; Blaaderen, A. v. Extended sedimentation profiles in charged colloids: the gravitational length, entropy, and electrostatics. *J. Phys.: Condens. Matter* **2005**, *17*, 2315–2326.

(54) Dinsmore, A. D.; Levitt, A. C.; Weitz, D. A.; Weeks, E. R.; Prasad, V. Three-dimensional confocal microscopy of colloids. *Appl. Opt.* **2001**, *40*, 4152.

(55) Edmond, K. V.; Elsesser, M. T.; Hunter, G. L.; Pine, D. J.; Weeks, E. R. Decoupling of rotational and translational diffusion in supercooled colloidal fluids. *Proc. Natl. Acad. Sci. U.S.A.* **2012**, *109*, 17891–17896.

(56) Savin, T.; Doyle, P. S. Static and dynamic errors in particle tracking microrheology. *Biophys. J.* **2005**, *88*, 623–638.

(57) Cavagna, A. Supercooled liquids for pedestrians. *Phys. Rep.* **2009**, *476*, 51–124.